

MAGAO IMAGING OF LONG-PERIOD OBJECTS (MILO). I. A BENCHMARK M DWARF COMPANION EXCITING A MASSIVE PLANET AROUND THE SUN-LIKE STAR HD 7449*

TIMOTHY J. RODIGAS^{1,12}, PAMELA ARRIAGADA¹, JACKIE FAHERTY¹, GUILLEM ANGLADA-ESCUDE², NATHAN KAIB³, R. PAUL BUTLER¹, STEPHEN SHECTMAN⁴, ALYCIA WEINBERGER¹, JARED R. MALES^{5,13}, KATIE M. MORZINSKI⁵, LAIRD M. CLOSE⁵, PHILIP M. HINZ⁵, JEFFREY D. CRANE⁴, IAN THOMPSON⁴, JOHANNA TESKE¹, MATÍAS DÍAZ^{4,6}, DANTE MINNITI^{7,8,9}, MERCEDES LOPEZ-MORALES¹⁰, FRED C. ADAMS¹¹, ALAN P. BOSS¹

Draft version January 1, 2019

ABSTRACT

We present high-contrast Magellan adaptive optics (MagAO) images of HD 7449, a Sun-like star with one planet and a long-term radial velocity (RV) trend. We unambiguously detect the source of the long-term trend from 0.6-2.15 μm at a separation of $\sim 0''.54$. We use the object's colors and spectral energy distribution to show that it is most likely an M4-M5 dwarf (mass $\sim 0.1\text{-}0.2 M_{\odot}$) at the same distance as the primary and is therefore likely bound. We also present new RVs measured with the Magellan/MIKE and PFS spectrometers and compile these with archival data from CORALIE and HARPS. We use a new Markov chain Monte Carlo procedure to constrain both the mass ($> 0.17 M_{\odot}$ at 99% confidence) and semimajor axis (~ 18 AU) of the M dwarf companion (HD 7449B). We also refine the parameters of the known massive planet (HD 7449Ab), finding that its minimum mass is $7.8^{+3.7}_{-1.35} M_J$, its semimajor axis is $2.33^{+0.01}_{-0.02}$ AU, and its eccentricity is $0.8^{+0.08}_{-0.06}$. We use N-body simulations to constrain the eccentricity of HD 7449B to $\lesssim 0.5$. The M dwarf may be inducing Kozai oscillations on the planet, explaining its high eccentricity. If this is the case and its orbit was initially circular, the mass of the planet would need to be $\lesssim 10.8 M_J$. This demonstrates that strong constraints on known planets can be made using direct observations of otherwise undetectable long-period companions.

Subject headings: instrumentation: adaptive optics — techniques: high angular resolution — techniques: radial velocity — stars: individual (HD 7449) — binaries — planetary systems

1. INTRODUCTION

Direct imaging and radial velocity (RV) are complementary planet detection techniques. RV is typically sensitive to gas giant planets orbiting within ~ 5 AU of old, Sun-like, chromospherically quiet stars. Direct imaging can detect super-Jovian planets orbiting beyond ~ 10 AU of young, massive stars. Stars with systems that bridge

the desired characteristics of the two methods are thus ideal targets for both RV and imaging.

The most obvious candidates are stars that show long-term RV trends, which indicate the presence of one or more massive companions on long-period orbits. Because imaging contrast improves far from the star's point spread function (PSF), such objects are ideal targets for imaging. The combined power of RV and direct imaging has been realized on several systems to date. A few M dwarfs have been imaged within 25 AU of stars that also host eccentric planets (Neuhäuser et al. 2007; Chauvin et al. 2011; Lagrange et al. 2006; Howard et al. 2010). Schnupp et al. (2010) directly imaged an M dwarf companion to a star that showed a long-term RV signal and used the derived photometric mass to constrain the system inclination. The TRENDS survey (Crepp et al. 2012, 2013a,b; Montet et al. 2014; Crepp et al. 2014) is specifically dedicated to targeting stars that have long-period RV trends. Several stellar and substellar companions have been discovered and characterized, helping to constrain the atmospheres of cool objects. This is especially relevant given the growing number of cool substellar and planetary mass objects being discovered by direct imaging. Even null-detections are useful, as Janson et al. (2009) and Rodigas et al. (2011) used 4 μm thermal imaging to set strong constraints on the types of substellar companions that could orbit two nearby stars.

We are conducting an adaptive optics (AO) direct imaging survey of nearby southern-hemisphere stars that have long-term RV trends. The stars are se-

* This paper includes data obtained at the 6.5 m Magellan Telescopes located at Las Campanas Observatory, Chile.

¹ Department of Terrestrial Magnetism, Carnegie Institute of Washington, 5241 Broad Branch Road, NW, Washington, DC 20015, USA; email: trodigas@carnegiescience.edu

² School of Physics and Astronomy, Queen Mary, University of London, 327 Mile End Rd. London, UK

³ Homer L. Dodge Department of Physics and Astronomy, The University of Oklahoma, 440 W. Brooks St. Norman, OK 73019, USA

⁴ The Observatories of the Carnegie Institution of Washington, 813 Santa Barbara Street, Pasadena, CA 91101, USA

⁵ Steward Observatory, The University of Arizona, 933 N. Cherry Ave., Tucson, AZ 85721, USA

⁶ Universidad de Chile, Departamento de Astronomía, Camino El Observatorio 1515, Las Condes, Santiago, Chile.

⁷ Departamento de Ciencias Físicas, Universidad Andres Bello, Campus La Casona, Fernández Concha 700, Santiago, Chile

⁸ Millennium Institute of Astrophysics, Av. Vicuña Mackenna 4860, 782-0436 Macul, Santiago, Chile

⁹ Vatican Observatory, Vatican City State, I-00120, Italy

¹⁰ Harvard-Smithsonian Center for Astrophysics, 60 Garden Street, Cambridge, MA 01238, USA

¹¹ Physics Department, University of Michigan, Ann Arbor, MI 48109, U.S.A.; Astronomy Department, University of Michigan, Ann Arbor, MI 48109, USA

¹² Hubble Fellow

¹³ NASA Sagan Fellow

lected from the combined RV planet surveys using the AAT/UCLES, Magellan/MIKE (Bernstein et al. 2003), and Magellan/PFS (Crane et al. 2010) instruments. The imaging is performed using the Magellan adaptive optics system (MagAO, Close et al. 2010), which offers simultaneous high Strehl ratio imaging in the visible (with VisAO, Kopon et al. 2010) and the infrared (with Clio-2, Sivanandam et al. 2006). The ability to image in the visible is a key advantage compared to other AO-enabled telescopes because an imaged object’s spectral energy distribution (SED) can then be constructed in a single night.

In this first paper, we report our observations of the Sun-like star HD 7449 located $38.9^{+0.74}_{-0.71}$ pc away (van Leeuwen 2007). HD 7449 is thought to be a sub-solar metallicity ($[F_e/H] = -0.11 \pm 0.01$, Dumusque et al. 2011, in agreement with Delgado Mena et al. 2015 and Santos et al. 2013) F8V star. Its age is estimated as 2.10 ± 0.24 Gyr old (Dumusque et al. 2011) based on the age-activity relations from Mamajek & Hillenbrand (2008). Dumusque et al. (2011) used HARPS and CORALIE RV data to suggest that HD 7449 has a planet with mass $> 1.1 M_J$ at 2.3 AU and a long-term trend, which they concluded was most likely arising from a planet with mass $> 2 M_J$ at 5 AU. The preferred orbits of these planets were very eccentric. Wittenmyer et al. (2013) searched for solutions containing two planets on near-circular orbits because such systems can often be mistaken for systems with only a single eccentric planet (Rodigas & Hinz 2009; Anglada-Escudé et al. 2010). They preferred solutions of a planet with mass $> 1.2 M_J$ at 2.83 AU and a second planet with mass $> 0.4 M_J$ at 1.44 AU, both with near-circular orbits.

Speckle interferometry searches for substellar companions close to the star have to date resulted in null-detections (Mason et al. 2011). Using MagAO’s simultaneous visible and infrared imaging capabilities coupled with high Strehl ratio AO, we have detected a faint object at a projected separation of $\sim 0''.54$ around HD 7449. In Section 2 we describe our observations, which include both imaging at seven wavelengths from 0.63-2.15 μm and new Doppler spectroscopy, and we describe our data reduction. In Section 3 we present photometry and astrometry for the object and show that it is an M dwarf at the same distance as the primary and thus is likely the source of the long-period trend; we also constrain its mass and period from RV analysis and provide updated parameters on the known inner planet HD 7449Ab; and we use numerical N-body simulations to further constrain the architecture of the system. In Section 4 we discuss the implications of our results, compare HD 7449 to other similar systems, and conclude.

2. OBSERVATIONS AND DATA REDUCTION

2.1. MagAO Imaging

We observed HD 7449 using the Magellan Clay Telescope at the Las Campanas Observatory in Chile on the nights of UT November 5, 2014 and November 22, 2014. We used MagAO paired with VisAO and Clio-2, for which we used the narrow camera (plate scale = $0''.01585$; Morzinski et al. 2015). On the first night, the observing conditions were fair, with seeing varying around $1''$, therefore only 200 modes of AO correction

were employed. We observed the star with VisAO at Y_s (0.99 μm) and with Clio-2 at H (1.65 μm) and K_s (2.15 μm). Unsaturated photometric images were also acquired in each filter. On the second night, the seeing was much better, with stable seeing under $1''$, therefore the maximum 300 modes of AO correction were employed. We observed the star with VisAO at r' (0.63 μm), i' (0.77 μm), z' (0.91 μm), and with Clio-2 at J (1.1 μm). Unsaturated photometric images were acquired in each filter. All observations were acquired with the instrument rotator off to enable angular differential imaging (ADI, Marois et al. 2006).

A bright object was identifiable in the raw images at each wavelength, separated by $\sim 0''.5$ from the star. Therefore ADI PSF subtraction was not needed to enhance contrast, and little integration was required in each filter. We obtained total integrations of 2.3 minutes at r' , 1.2 minutes at i' , 1.17 minutes at z' , 1.9 minutes at Y_s , 0.5 minutes at H , 18.67 minutes at J , and 4.33 minutes at K_s .

All data reduction was performed with custom scripts in Matlab. The Clio-2 images were divided by the number of coadds, corrected for nonlinearity (Morzinski et al. 2015), divided by the integration times, sky-subtracted, and then registered and cropped. The VisAO images were dark-subtracted, divided by the integration times, and then registered and cropped. All images were rotated to North-up, East-left and then median-combined into final images at each wavelength. Finally, 2D radial profiles were subtracted from each image to remove the majority of the stellar flux (see Fig. 1). The object at $\sim 0''.54$ is unambiguously detected in each filter.

2.2. Doppler Spectroscopy

RV data on HD 7449 were first acquired as part of the Magellan Planet Search Program, which originally made use of the MIKE echelle spectrometer (Bernstein et al. 2003) on the Magellan Clay telescope until September 2009. The reported precision achieved by MIKE was

TABLE 1
RVs FOR HD 7449

Julian Date	RV (m/s)	σ_{RV} (m/s)	Instrument
2451459.55882	78.57	10.00	1
2451480.14706	86.90	10.00	1
2451490.44118	76.19	10.00	1
2451541.91176	76.90	10.00	1
2451747.79412	52.62	10.00	1
...			

Notes. Table 1 is published in its entirety in the electronic edition of XXX. A portion is shown here for guidance regarding its form and content. Instrument 1 corresponds to CORALIE (Dumusque et al. 2011), 2 corresponds to HARPS, 3 corresponds to Magellan/MIKE, and 4 corresponds to Magellan/PFS.

5 ms^{-1} on solar type stars (Minniti et al. 2009). Observations with MIKE were made using a $0''.35$ slit, which results in a spectral resolution of $R \sim 70,000$ in the blue and $\sim 50,000$ in the red. The wavelength coverage ranges from 3900 to 6200 \AA , capturing the iodine region (5000-6300 \AA), and is divided into two CCDs covering the red and blue wavelength regions.

HD 7449 was subsequently observed using the Carnegie Planet Finder Spectrograph (PFS, Crane et al. 2010),

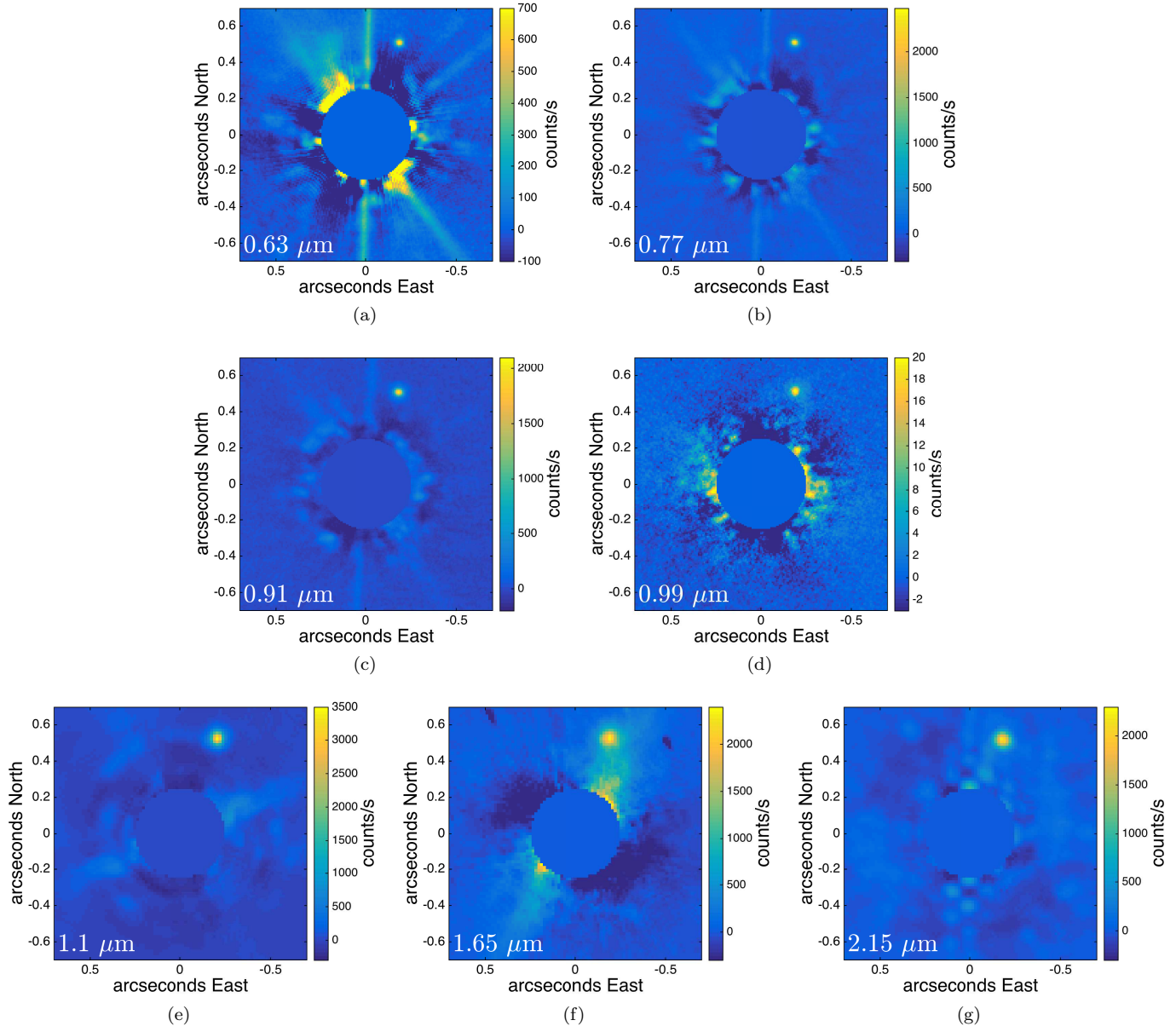


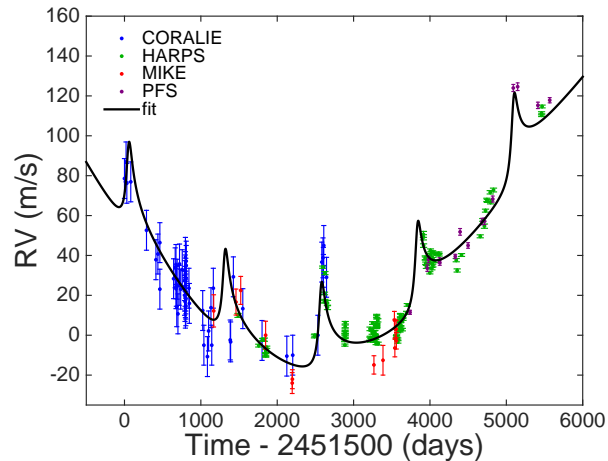
FIG. 1.— Final reduced images of HD 7449 and its outer companion at seven photometric bands with central wavelengths noted on the panels: r' (a), i' (b), z' (c), Ys (d), J (e), H (f), and Ks (g). North is up and East is to the left, and a $0''.25$ radius digital mask around the star has been added for display purposes. Radial profiles have been subtracted from each image to remove the stellar halos, since no PSF subtraction was performed. The companion is clearly visible at a separation of $\sim 0''.54$ and position angle ($P.A.$) of $\sim 340^\circ$.

a temperature-controlled high resolution spectrograph, which now carries out all observations for the Magellan Planet Search Program. PFS covers 3880 to 6680 \AA and the $0''.5$ slit is used, which results in a spectral resolution of $\sim 80,000$ in the iodine region. Continuous monitoring of stable stars reveals that the Magellan/PFS system achieves an average measurement precision of 1.5 ms^{-1} (Arriagada et al. 2013).

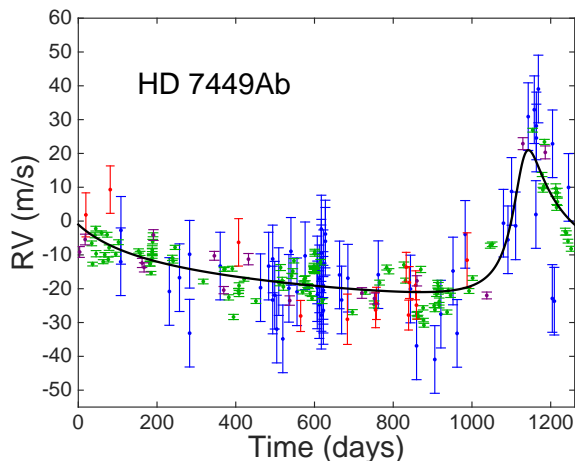
The RVs for both instruments were obtained using the iodine technique (Butler et al. 1996). Briefly, an iodine absorption cell provides the wavelength scale and instrumental PSF for each stellar observation, which are computed in 2 \AA chunks. A forward modeling procedure of each observation is carried out for each chunk, thus providing an individual measurement of the wavelength, PSF, and Doppler shift. The final measured RV is the

weighted average of all the chunks for a given observation. Internal uncertainties are computed as the standard deviation of the velocities derived from each chunk. The new RVs for HD 7449 obtained from MIKE and PFS are listed in Table 1.

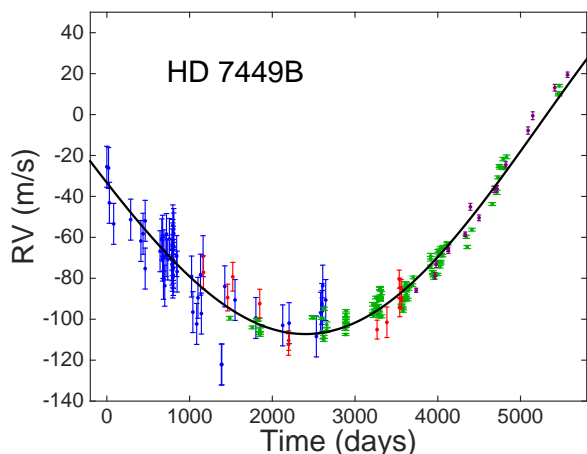
We also included in our analysis RVs measured with HARPS and CORALIE. These RVs were originally reported in Dumusque et al. (2011). However, HD 7449 has been observed by HARPS since that publication, so we downloaded all available HARPS data on HD 7449 from the ESO archive. Starting from the ESO extracted and calibrated spectra, we obtained new Doppler measurements using the HARPS-TERRA software (Anglada-Escudé & Butler 2012). The CORALIE data were not explicitly reported by Dumusque et al. (2011), nor are they available in any archive, so we



(a)



(b)



(c)

FIG. 2.— RVs for HD 7449. Blue, green, red, and purple points correspond to CORALIE (Dumusque et al. 2011), HARPS, and Magellan/MIKE and PFS, respectively. (a) The RV data and the combined best-fit (solid black line). (b-c) The phase-folded RV data and fits to the two strongest signals, the massive planet on a very eccentric orbit (HD 7449Ab) and the long-period companion (HD 7449B), with the other signals removed in each case.

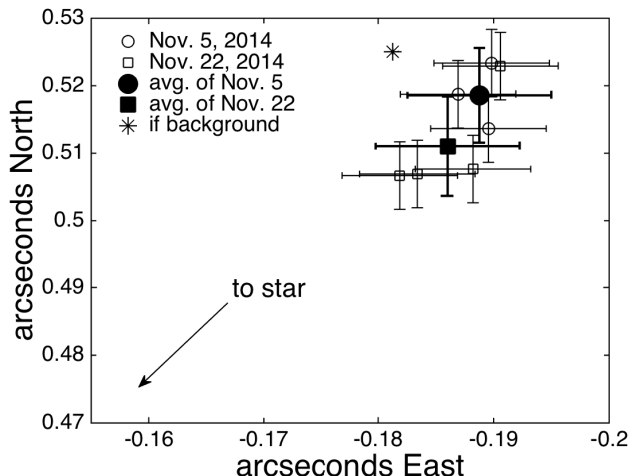


FIG. 3.— Astrometry of HD 7449B from our two epochs of MagAO imaging. The circles correspond to the detections on Nov. 5, 2014 and the squares correspond to Nov. 22, 2014. The asterisk denotes where the companion would have been located on Nov. 22, 2014 if it were a background object, based on the star’s proper motion (van Leeuwen 2007). The object’s motion over 17 days is inconsistent with a background object at the 2σ confidence level.

used *DataThief* (<http://datathief.org>) to retrieve the RVs. To account for possible errors in the extraction, we assumed 10 ms^{-1} errors for the CORALIE data in our subsequent RV analysis. The entire RV data set is shown in Fig. 2a, revealing the clear long-term, parabolic trend, and the individual RVs are reported in Table 1.

3. RESULTS

3.1. Outer Companion Photometry and Astrometry

Photometry was measured as follows. First, a circular aperture of radius = 1 full-width half-maximum (FWHM), corresponding to the size of a diffraction-limited PSF at each wavelength, was placed at the detected object’s photocenter in each image. The same aperture was placed at the stellar photocenter in each unsaturated image, and then the fluxes within all the apertures were summed. Uncertainties were calculated as the standard deviations of the fluxes in apertures placed around the star at the same radius.

Astrometry was measured by calculating the photocenters in the same apertures, and astrometric uncertainties were assumed to be 5 mas at each wavelength based on previous imaging with MagAO (e.g., Rodigas et al. 2015). Table 2 lists the object’s photometry and astrometry. The object has a separation of $\sim 0''.54$ and $P.A. \sim 340^\circ$. Because the star has high proper motion (van Leeuwen 2007), the two epochs of direct detections separated by only 17 days is enough to show that the object is inconsistent with being background at 2σ confidence. In Section 3.2, we will show that the object’s SED confirms that it is unlikely to be background.

Henceforth, we will refer to the outer object as HD 7449B. Note that Roell et al. (2012) suggest that HD 7449 has a common proper motion companion at > 2000 AU. The candidate companion was identified using the PPMXL proper motion catalog (Roeser et al. 2010). Examining the relevant images from PPMXL reveals that the object is actually one of the diffraction spikes and is therefore not a real astrophysical source. Therefore HD

TABLE 2
HD 7449B PHOTOMETRY AND ASTROMETRY

Parameter	Value
$\Delta r'$ (0.63 μm)	$8.82^{+0.13}_{-0.11}$
$\Delta i'$ (0.77 μm)	$7.32^{+0.13}_{-0.11}$
$\Delta z'$ (0.91 μm)	$6.53^{+0.15}_{-0.13}$
ΔY_s (0.99 μm)	$5.87^{+0.23}_{-0.23}$
ΔJ_{MKO} (1.1 μm)	$5.81^{+0.11}_{-0.10}$
ΔH_{MKO} (1.65 μm)	$5.11^{+0.11}_{-0.10}$
ΔK_{SBarr} (2.15 μm)	$4.85^{+0.03}_{-0.03}$
$M_{r'}$	13.39 ± 0.17
$M_{i'}$	11.51 ± 0.17
$M_{z'}$	10.75 ± 0.20
M_J	9.26 ± 0.16
M_H	8.33 ± 0.16
M_{K_s}	7.97 ± 0.09
ΔRA_{t_1} (")	-0.19 ± 0.003
ΔDec_{t_1} (")	0.52 ± 0.003
ΔRA_{t_2} (")	-0.19 ± 0.006
ΔDec_{t_2} (")	0.51 ± 0.005
ρ_{t_1} (")	0.55 ± 0.007
$P.A._{t_1}$ ($^\circ$)	339.99 ± 1.84
ρ_{t_2} (")	0.54 ± 0.007
$P.A._{t_2}$ ($^\circ$)	339.99 ± 1.88

Notes. $t_1 =$ UT Nov. 5, 2014; $t_2 =$ UT Nov. 22, 2014. M_{Y_s} is not reported (or used in any photometric analysis) because the primary star has no reported measurements near 1 μm .

7449 does not have any stellar companions at > 2000 AU.

3.2. Outer Companion Mass from Photometry

Because we have detections of HD 7449B in both the visible and the near-infrared (NIR), we can use its colors and absolute magnitudes to constrain its spectral type, effective temperature (T_{eff}), and mass. To accomplish this, we compared its photometry to both known objects and to the low-mass stellar models of Kraus & Hillenbrand (2007) and Baraffe (Baraffe et al. 1998, 2002, 2015).

To create a comparative SED for HD 7449B, we began with the MagAO photometry for the primary and the outer companion. We used catalog 2MASS and SDSS photometry for HD 7449A and then used the color transformation relations in Carpenter (2001) to put the NIR photometry on the MKO system, which is comparable to the MagAO filters. Photometry for HD 7449B was then obtained by computing the magnitude differences relative to the primary. We used the Hipparcos parallax of 25.69 ± 0.48 mas (van Leeuwen 2007) to compute the absolute magnitudes and then converted each to λF_λ (e.g., see Faherty et al. (2013)). Fig. 4 shows the resulting SED for HD7449B as well as the similarly-computed SEDs of comparative M dwarfs from the 8-parsec sample (Reid & Gizis 1997). The best matching SED corresponds to an M4.5, which also confirms that HD 7449B is at the distance to the primary (38.9 pc).

To demonstrate that HD 7449A and B fall along the main sequence together (hence verifying that they are likely co-eval), we constructed color magnitude diagrams (CMDs) at several wavelengths from the visible to the NIR. We used the low-mass star Hipparcos sample, the NSTARS parallax sample, and the brown dwarf parallax sample from Dupuy & Liu (2012) and Faherty et al. (2012). Because these report photometry in the 2MASS

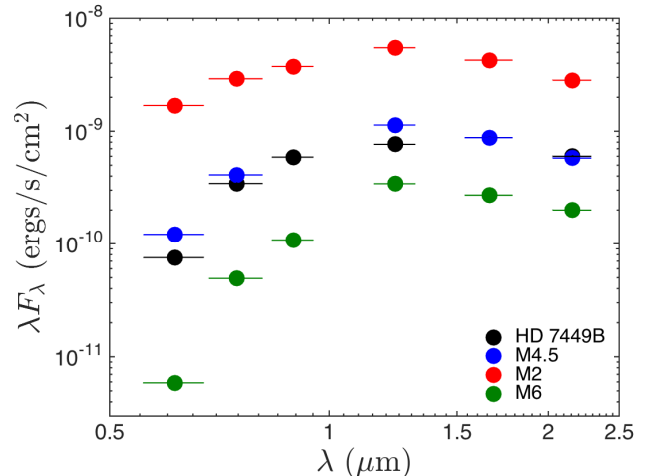


FIG. 4.— SED of HD 7449B, along with other M dwarfs. Error bars are smaller than the marker sizes. The companion's SED point at Y_s is not shown because HD 7449A has no measured flux at this wavelength. The companion's SED point at H lies behind the point corresponding to the M4.5, which itself has no z' flux measurement. HD 7449B is most similar to the M4.5 source. This also confirms that it is likely to be at the distance to the primary (38.9 pc).

system, we converted our MagAO photometry to 2MASS (assuming MKO comparable) using the Carpenter (2001) relations. All CMDs generally showed that the A and B components fall on the main sequence together, indicating that they are co-eval and that the companion is not a background or foreground object. Fig. 5 shows an example CMD.

Using the Kraus & Hillenbrand (2007) models, comparing HD 7449B's colors and absolute magnitudes yielded a best-matching spectral type of M5, $T_{eff} = 3010K$, and $M = 0.15M_\odot$. Using the pre-2015 Baraffe models (Baraffe et al. 1998, 2002), and assuming the stellar age is between 1-3 Gyr, the colors were best matched by a $0.10 M_\odot$, $T_{eff} = 2824K$, 1 Gyr old star. The absolute magnitudes were best matched by a $0.15 M_\odot$, $T_{eff} = 3161K$, 1 Gyr old star. Using the 2015 Baraffe models, for stellar ages between 1-3 Gyr, the colors were best matched by a star with $M = 0.20 M_\odot$, $T_{eff} = 3261K$, and the absolute magnitudes were best matched by a star with $M = 0.09 M_\odot$ and $T_{eff} = 2643K$. Based on all of the above analysis, we classify HD 7449B (from photometry alone) as an $M4.5 \pm 0.5$ with mass = $0.15 \pm 0.05M_\odot$.

3.3. Constraints from RV Fitting

RVs have been obtained on HD 7449 for the past ~ 15 years by HARPS and CORALIE (Dumusque et al. 2011), and by Magellan/MIKE and PFS (this work; see Table 1). To explain the periodic RVs (and the clear long-term trend), previous works (Dumusque et al. 2011; Wittenmyer et al. 2013) searched for solutions explained by one or more planets. We have the advantage that we know from direct imaging that the system contains an $\sim M4.5$ companion whose current projected separation is $\gtrsim 21$ AU. Can this companion explain the long-term trend and in doing so help revise the parameters of the inner planet(s)?

To test this, we first analyzed the RVs using log-likelihood periodograms (Baluev 2009;

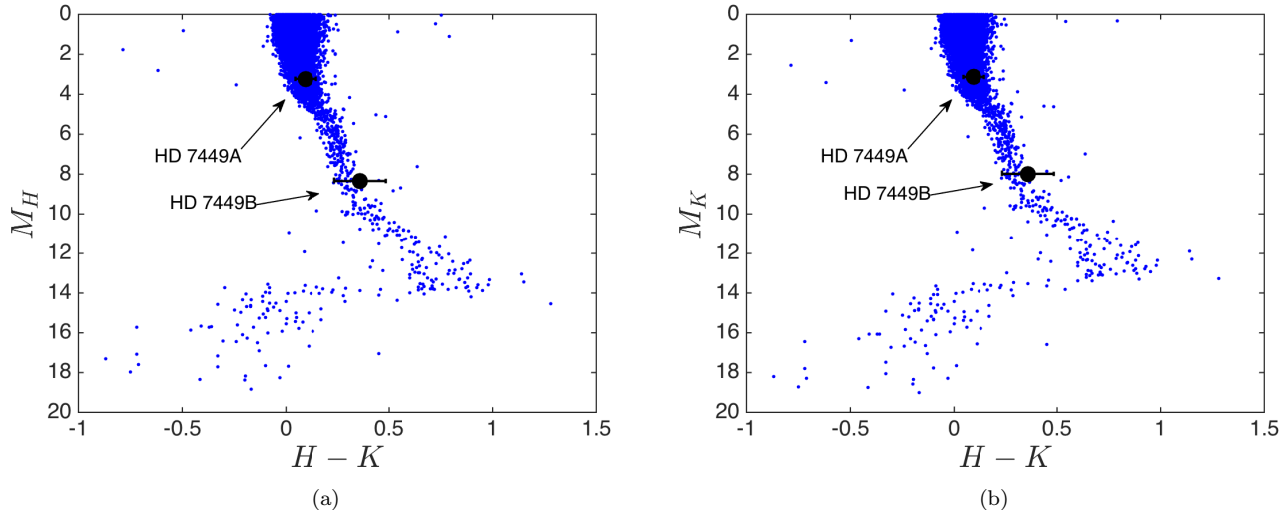


FIG. 5.— NIR CMDs for HD 7449A and B (black points). Blue points correspond to cool stars and brown dwarfs from the Hipparcos, NSTARS, Dupuy & Liu (2012), and Faherty et al. (2012) samples. These CMDs show that the A and B components fall on the main sequence together, which means they are likely to be co-eval. Therefore HD 7449B is unlikely to be a background object.

Anglada-Escudé et al. 2014) for preliminary period detection and confidence evaluation. Then we used a Bayesian Markov Chain Monte Carlo (MCMC) approach to produce posterior distributions of the allowed parameter values (Ford 2005). The likelihood function L contains the Keplerian model and a handful of nuisance parameters to account for the arbitrary zero-points of each RV instrument and the different levels of instrumental excess noise (also called jitter, which typically contains the contribution from stellar activity). The likelihood function is given by

$$L = \prod_I \prod_i^{N_{obs}} l_{i,I} \quad (1)$$

$$l_{i,I} = \frac{1}{\sqrt{2\pi}} \frac{1}{\sqrt{\epsilon_{i,I}^2 + s_I^2}} \exp \left[-\frac{1}{2} \frac{(v_{i,I} - v(t, I))^2}{\epsilon_{i,I}^2 + s_I^2} \right] \quad (2)$$

$$v_{i,I} = \gamma_I + \sum_p u(\hat{\kappa}_p; t) + \dot{v}_r(t - t_0) + \frac{1}{2} \ddot{v}_r(t - t_0)^2, \quad (3)$$

where i indexes the observations acquired with the I th instrument, $\epsilon_{i,I}$ is the nominal uncertainty of each RV measurement, γ_I and s_I are the zero-point and extra noise parameters (also called jitter) of each instrument, and the Doppler signal from a companion on the star is encoded in the model $u(\hat{\kappa}_p; t)$, which is a function of time t and the Keplerian parameters $\hat{\kappa}_p$. The Keplerian parameters of the p^{th} companion in the system are: the orbital period P_p (in days), the semi-amplitude K_p (in m/s), the mean anomaly $\mu_{0,p}$ at the reference epoch t_0 (in degrees), the eccentricity e_p , and the argument of periastron ω_p . The second and third terms in Eq. 3 account for the possible presence of a long-period candidate whose orbit is only detected as a trend (acceleration, \dot{v}_r) plus some curvature (jerk, \ddot{v}_r). These two terms are especially important for the analysis that follows.

When performing the Bayesian MCMC analysis, one

needs to specify some prior distributions for these parameters. In this paper, we use uniform distributions for the angles μ_0 and ω , as any value would be equally likely a priori. Given that the objects involved are rather massive and the signals large, we also allow for a uniform eccentricity distribution between $[0, 0.95]$. For K_p , γ_I , s_I , \dot{v}_r , and \ddot{v}_r , we assume unbound non-normalized uniform priors. While this can cause issues when normalizing the posterior, we are only using the MCMC analysis to sample the *shape* of the posterior, so precise values of the bounds and the normalization factors are unnecessary. Furthermore, because we will later try to constrain the signal with a period much longer than the span of the observations, the possible values of these three quantities will be correlated, so bound priors might eliminate many long period solutions that would otherwise be highly probable. For example, a large K in general requires a large γ unless the companion is precisely crossing the plane of the sky at t_0 (which is highly unlikely).

Regarding the prior on the period, in this work we assume that the prior is uniform in $1/P$ (equivalent to uniform in frequency). This is motivated by the following. When analyzing time series, the local solutions to periodic signals are approximately equally-spaced in frequency. For example, if one produces a Lomb-Scargle periodogram of a time series and plots period versus power, one will quickly appreciate that the peaks become much broader with increasing period (Scargle 1982). However, when making the same plot in frequency, the peaks appear uniformly distributed over the possible frequencies. As discussed in Tuomi & Anglada-Escudé (2013), in Bayesian statistics the choice of the parameter automatically imposes implicit priors on all other alternative parameterizations. In the case of the period, a uniform prior at very long periods can outweigh the information content on the likelihood, producing a biased result. While this issue is not very severe for periods shorter than the time-span of the observations (typical RV planet search domains), the disrupting effects of the uniform prior become serious if one attempts to constrain

very long orbits and becomes strongly dominated by the chosen period cut-off. On the other hand, the frequency parameter does not suffer from such singularities (all very long periods become packed in a single likelihood maxima close to 0) and preserves the role of the likelihood function as the most informative element in the posterior distribution.

Our MCMC algorithm is based on the one described in Ford (2005), which uses a Gibbs sampler with independent Gaussian jump functions for each parameter. For each parameter, the proposal function of our Gibbs sampler depends on a scale parameter that needs to be tuned to ensure acceptance rates between 10% and 30%. This is automatically done by tuning all the scale parameters until they reach the aforementioned acceptance rates (burn-in period). These samples typically amount for 10^6 iterations and they are not used for the final MCMC analysis. In this paper we only focus on the detection and characterization of the two most significant signals in the RV data (HD 7994Ab and the long-period trend). While there have been other claims of possible candidates in the system (Dumusque et al. 2011; Wittenmyer et al. 2013), we suspect these were artifacts caused by sampling issues with the rather eccentric orbit of HD 7994Ab and the presence of the long-period parabolic trend.

3.4. Two Planet MCMC

Our first analysis consisted of a likelihood function with two Keplerian signals: one initialized at $P \sim 1200$ days (which roughly corresponds to the preferred period for the most significant planet in Dumusque et al. 2011 and Wittenmyer et al. 2013), and the other one at $P \sim 8000$ days, as suggested by the maximum likelihood periodograms in Fig. 6. While a maximum likelihood orbit could be obtained with a second planet at $\sim 10,000$ days (30 years), long MCMC runs indicated that the possible parameters of this object were heavily correlated. As a result, the parameter space was broadly unconstrained, making it difficult for the chains to achieve convergence even after 10^8 - 10^9 steps. Such strong degeneracy indicates that only a subset of the 5 Keplerian parameters can be constrained by the current data. As we will see later, the trend in the RV data can be well-described by two terms: an acceleration (linear trend) + jerk (curvature).

3.5. Two Planet MCMC with Imaging Constraints

As an attempt at better constraining the orbital elements of the outer companion, in our second analysis we included a Keplerian model for the outer companion's predicted orbital separation in order to use our direct imaging constraints (e.g., see Lucy 2014). Unfortunately, the orbital motion of the imaged companion was not very large between the direct imaging runs, and the imaging provides just two observables (projected separation in RA and Dec) while introducing three more free parameters (orbital inclination i , longitude of ascending node Ω , and the mass ratio between the companion and the primary star). As a result, these MCMC chains had even more difficulty converging to a meaningful equilibrium distribution (e.g., companion masses up to $100 M_\odot$ and periods up to millions of years were consistent with the data).

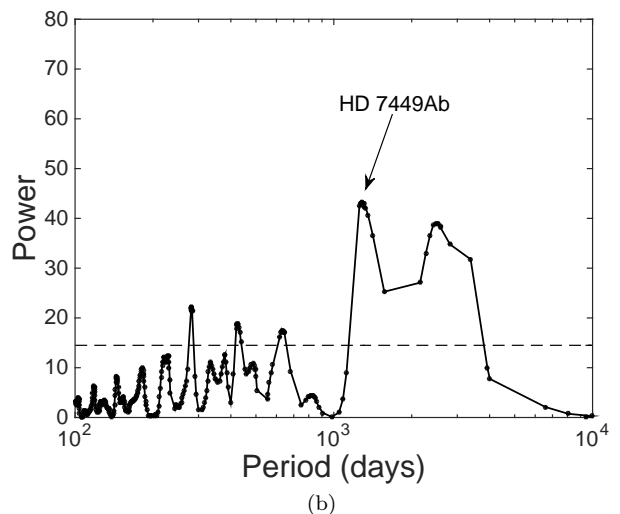
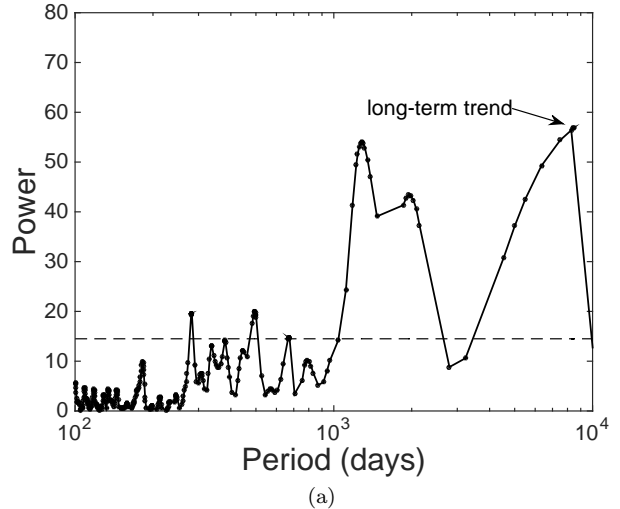


FIG. 6.— Periodograms for the HD 7449 RV data. The dashed line corresponds to the 1 percent false-alarm probability threshold. (a) First periodogram used to identify the strongest signal, which corresponds to the long-period companion. Its period is likely to be > 8000 days. (b) Second periodogram used to identify the next strongest signal at ~ 1200 days, corresponding to the previously-identified HD 7449Ab.

3.6. One Planet MCMC + Long-period terms

Given that the entire RV data set (including HARPS, CORALIE, MIKE, and PFS RVs) can be well-fit by a simple parabola, for our third analysis we implemented a Doppler model containing a single inner planet plus a linear and quadratic term. In this case, the model contains a single Keplerian initialized at 1200 days (inner planet), plus the last two terms in Eq. 3. Since \dot{v}_r and \ddot{v}_r are linear parameters, the MCMC quickly converged to the best-fit solution, which had an almost identical value of the likelihood function to the full two Keplerian solution attempted in Section 3.4. This means that the entire RV data set is best (and most simply) described by a single inner planet along with a long-term trend consisting of linear plus quadratic terms. We therefore use this final MCMC's results to constrain the parameters of the companions around HD 7449.

The posterior distributions of the inner planet's pa-

parameters are shown in Fig. 7. Clearly, HD 7449Ab is eccentric (median $e_b = 0.8$), in agreement with Dumusque et al. (2011). To constrain the planet’s mass (m), we used the distributions of K_b , P_b , and e_b , drew random Gaussian-distributed values for the stellar mass M_* having mean = $1.05 M_\odot$ and standard deviation = $0.09 M_\odot$ ¹⁵, assumed $M_* \gg m$, and then solved for $m \sin i_b$ using the well-known relation

$$m \sin i_b = K_b \sqrt{1 - e_b^2} M_*^{2/3} \left(\frac{P_b}{2\pi G} \right)^{1/3}. \quad (4)$$

We find that the median $m \sin i_b = 7.8 M_J$, which is a bit more massive than the preferred mass found by Dumusque et al. (2011). HD 7449Ab’s parameters and their possible ranges are listed in Table 3.

3.7. Statistical Constraints on Outer Companion

Here we develop and apply a new statistical procedure, expanding on the one developed in Torres (1999), that uses the slope and quadratic terms discussed in Section 3.6 to tightly constrain the outer companion’s properties.

For the case of an imaged companion producing a long-period RV trend, Torres (1999) formulated a numerical Monte Carlo approach to marginalize over unknown parameters under some uninformative priors. It is based on using the fact that the linear trend observed in a Doppler curve of the primary star can be written in terms of the mass of the long-period companion only (M_B), and that the observed separation at a given epoch t_0 can be written as a function of M_B , the direct imaging observables, and a function that can be easily marginalized over the unknown orbital parameters (P_B , e_B , ω_B , $\mu_{0,B}$, i_B , Ω_B). The method described in Torres (1999) uses only the measured linear part of the trend and produces a distribution of possible masses. We now develop a method that exploits the second derivative of the RV (the jerk), which allows us to obtain a probability distribution for the companion’s orbital period as well. In this section, all the quantities refer to the secondary companion, so we will avoid using sub-indices for clarity, except for the period P_B and mass M_B of the secondary.

We begin with Equations (3) and (5) from Torres (1999) to write the derivative of the radial velocity of the primary component \dot{v}_r as

$$\dot{v}_r = \frac{GM_B}{\ell^2} \Psi, \quad (5)$$

$$\Psi = [(1 - e)(1 + \cos E)]^{-1} (1 - e \cos E) \sin i \times (1 - \sin^2(\nu + \omega) \sin^2 i) (1 + \cos \nu) \sin(\nu + \omega), \quad (6)$$

where ℓ is the projected separation between the primary star and the companion in physical units (e.g., mks), and Ψ is a rather intricate function that encapsulates all the orbital elements to be marginalized (time-dependencies included). Eq. 5 can be evaluated by solving Kepler’s equation

$$E - e \sin E = \mu \quad (7)$$

¹⁵ Dumusque et al. (2011) do not report an uncertainty on the stellar mass. Therefore we computed the average of four reported mass values and errors from Santos et al. (2013), Tsantaki et al. (2013), Bonfanti et al. (2015), and Pinheiro et al. (2014).

to obtain the eccentric anomaly E , and then using

$$\tan \frac{\nu}{2} = \sqrt{\frac{1+e}{1-e}} \tan \frac{E}{2} \quad (8)$$

to derive the true anomaly ν . To account for all possible combinations of periods and orbital phases, Torres (1999) realized that the mean anomaly $\mu = \frac{2\pi}{P_B} t + \mu_0$ could be assumed to be uniformly distributed in $(0, 2\pi]$. That is, irrespective of the values of the observation time t and P_B , μ still can be assumed to have any orbital phase because μ_0 can also have any value between 0 and 2π .

To use the information on the quadratic term in the RV curve, we first need to compute the second derivative of the RV. To do this efficiently, it is enough to realize that all the time dependence is included in μ . Therefore, we can apply the chain rule and the fact that $d\mu/dt = 2\pi/P_B$ to obtain

$$\ddot{v}_r = 2\pi \frac{G}{\ell^2} \frac{M_B}{P_B} \Psi' \quad (9)$$

$$\Psi' = \frac{d\Psi}{d\mu}. \quad (10)$$

This is an important result because we have found that \ddot{v}_r is proportional to M_B/P_B , and all the dependencies can again be marginalized by evaluating Ψ' (which is a function of time because it depends on E). While an analytic expression for Ψ' could be derived, it is far simpler (and requires fewer operations) to compute this numerically. We found that a simple two point formula with an infinitesimal increment of 10^{-4} radians for μ works to sufficient precision. By rearranging terms in Eq. 5 and combining Eq. 5 with Eq. 9, we find

$$\frac{M_B}{M_\odot} = 5.341 \times 10^{-6} \dot{v}_r \left(\frac{\rho}{\Pi} \right)^2 \frac{1}{\Psi}, \quad (11)$$

$$\frac{P_B}{yr} = 2\pi \frac{\dot{v}_r}{\ddot{v}_r} \frac{\Psi'}{\Psi}, \quad (12)$$

where ρ and Π are the projected separation and parallax in arcseconds, respectively. Eq. 11 was already derived in Torres (1999). The additional relation that we present here (Eq. 12) can be used to constrain a companion’s period using the same observables and marginalization method outlined in Torres (1999). The numerical factors in the equations come from the numerical substitution of the gravitational constant G , and the choice of units in Torres (1999), which assumes that \dot{v}_r is in $\text{m s}^{-1} \text{ yr}^{-1}$, and \ddot{v}_r is in $\text{m s}^{-1} \text{ yr}^{-2}$. Note that Eqs. 5 and 12 assume that we can produce a Taylor expansion of the RV near the epoch of the direct image(s). The most straightforward way to impose this condition is to set the reference epoch in Eq. 3 to $t_0 = t_{\text{image}}$, thus deriving consistent MCMC samples for \dot{v}_r . This consideration is unnecessary when no curvature is detectable in the RV curve, as the first derivative of the RV is then independent of time.

With Eqs. 5 and 12 in hand, we set out to constrain the mass and period of the outer companion. All the quantities have uncertainties, including \dot{v}_r , \ddot{v}_r , ρ , and Π . To account for these, we applied an additional refinement to the marginalization procedure of Torres (1999). That is, in addition to drawing random values for e , μ , and $\sin i_B$,

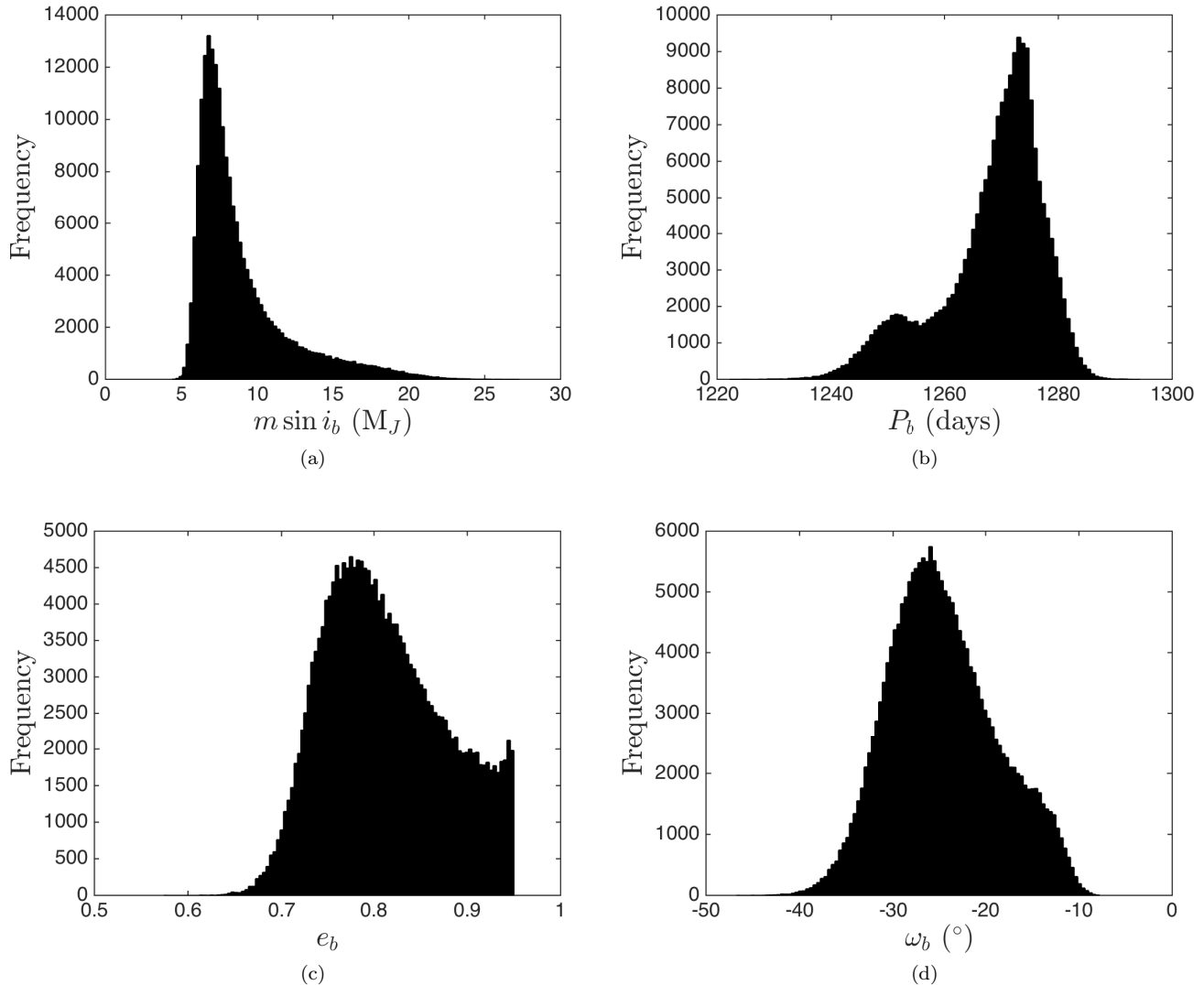


FIG. 7.— Marginalized posterior distributions of parameters for HD 7449Ab from our MCMC analysis (Section 3.6). (a) The planet’s minimum mass, $m \sin i_b$. (b) The planet’s period, P_b . (c) The planet’s eccentricity, e_b . (d) The planet’s argument of periastron, ω_b . The planet’s properties are tightly constrained: it is likely to be massive and very eccentric, perhaps indicating previous or ongoing dynamical interactions with the outer M dwarf companion (HD 7449B).

TABLE 3
HD 7449A COMPANION PARAMETERS

	Mass	Period	a (AU)	e	ω ($^\circ$)	i ($^\circ$)
HD 7449Ab	$> 7.8^{+3.7}_{-1.35} M_J$	$1270.5^{+5.92}_{-12.1}$ days	$2.33^{+0.01}_{-0.02}$	$0.80^{+0.08}_{-0.06}$	$-25.2^{+6.87}_{-5.22}$	unconstrained
HD 7449B	$0.23^{+0.22}_{-0.05} M_\odot$	65.7^{+227}_{-56} years	$17.9^{+32}_{-12.9}$	unconstrained	unconstrained	$59.7^{+20.1}_{-25.8}$

Notes. All uncertainties correspond to symmetric 68% confidence intervals around the median values.

we also drew randomly-generated values of the observables: \dot{v}_r and \ddot{v}_r pairs were drawn from randomly selected states of the MCMC, and Gaussian distributions consistent with the error on parallax and the error on projected separation (Table 2) were used to generate plausible pairs of Π and ρ , respectively. We know that the outer companion must be less massive than the primary (or it would be a known visual binary), so we excluded all parameters that corresponded to mass $> 1 M_\odot$. Sub-samples of the resulting distributions for the outer companion’s mass, period, and inclination are shown in Fig.

8. Based on these distributions, the median mass of HD 7449B is $0.23 M_\odot$, and the mass of HD 7449B is larger than $0.17 M_\odot$ with a 99% probability, consistent with our constraints from photometry. The median period is 65.7 years, corresponding to a semimajor axis of 17.9 AU. The inclination distribution is broad and has a median value of $i = 59.7^\circ$ because it is mostly inherited from the uniform distribution in the Monte Carlo generated test values. However, because we exclude masses larger than $1 M_\odot$, values of $i_B < 8.4^\circ$ are also excluded with 99% probability, thus ruling out strictly face-on orbits. We

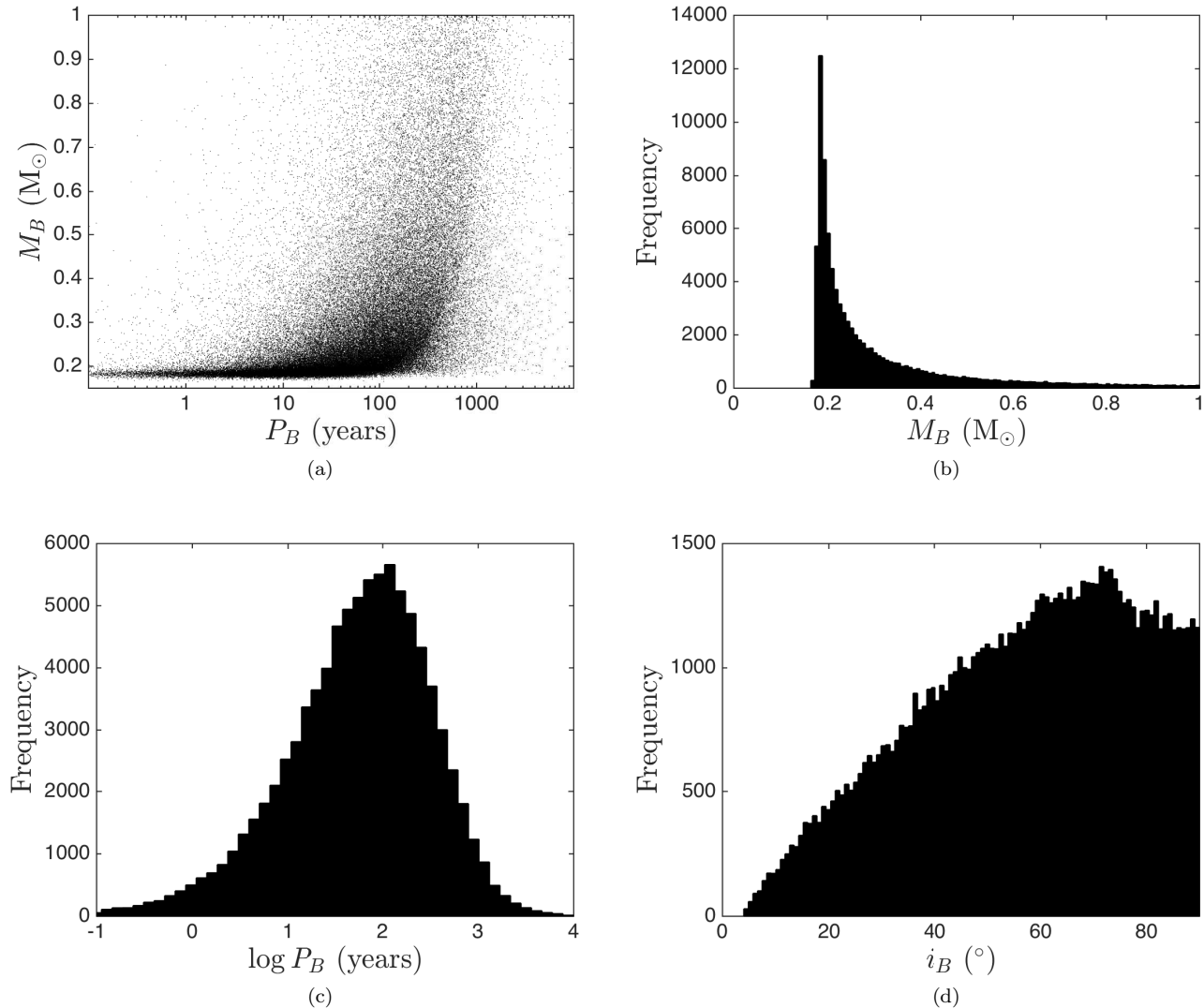


FIG. 8.— (a) Mass vs. period for the outer companion computed using the MCMC method described in Section 3.7. (b) Mass distribution for the outer companion from the analysis, showing a sharp peak near $\sim 0.2 M_{\odot}$. (c) log period distribution, showing a broad peak near ~ 65 years. (d) Inclination distribution, showing a general preference for larger i .

do not show the distributions for e and ω because they were completely unconstrained. Table 3 lists the outer companion’s constrained parameters and ranges.

3.8. Dynamical Constraints

Based on the above analysis, we were able to constrain the outer companion’s mass, period, and inclination, but not its eccentricity. To get a sense of the allowed ranges, we explored the dynamical stability of the system. We used the MERCURY integration package (Chambers 1999) with a Bulirsch-Stoer integrator and simulated 100 different realizations of the system for 1 Gyr. The initial semimajor axis and eccentricity of the inner planet (HD 7449Ab) were held fixed at 2.32 AU, and 0.78, respectively, while its mass was set to $7.67 M_J$ ¹⁶. The outer companion’s semimajor axis was fixed at 18 AU and we assumed near-coplanarity such that

its initial inclination relative to the planet was randomly drawn from values between 0 and 1° ¹⁷. In each of the 100 simulations, the companion’s eccentricity was varied between 0 and 1 in increments of 0.01. Its mass was set to $0.17 M_{\odot}$. For both the outer companion and the planet, the arguments of pericenter, longitudes of ascending node, and mean anomalies were all drawn randomly from a uniform distribution in each simulation.

In this case, the outer companion’s critical eccentricity e_{crit} (the eccentricity above which the planet’s orbit becomes unstable) was 0.45. Based on this initial result, we performed additional simulations in which the planet and outer companion had mutual inclinations $\Delta i = 30^\circ, 60^\circ, 90^\circ, 120^\circ, 150^\circ, \text{ and } 180^\circ$. For the 90° case, the planet was never stable regardless of the outer companion’s eccentricity. The critical eccentricities for the other inclinations were (in ascending order of mutual inclina-

¹⁶ These values are slightly smaller than the nominal values listed in Table 3 to ensure that the limits on dynamical stability are conservative.

¹⁷ A very small initial inclination was chosen to avoid making the calculation completely 2D, which would preclude any possible inclination growth.

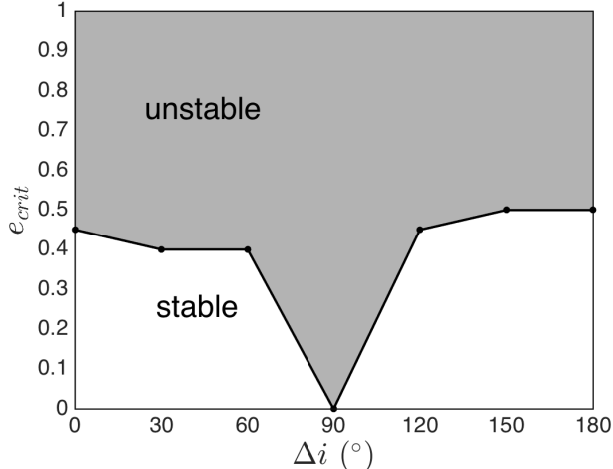


FIG. 9.— Results of the numerical N-body simulations for HD 7449. The eccentricity of HD 7449B is constrained to be $\lesssim 0.5$ for all mutual inclinations other than 90° , for which the system is never stable.

tion) 0.4, 0.4, 0.45, 0.5, and 0.5, respectively. Based on these results, the outer companion’s eccentricity is constrained to be $\lesssim 0.5$. Fig. 9 summarizes the results of our stability analysis.

4. DISCUSSION AND SUMMARY

We have directly imaged the source of the long-period trend in the RV data for HD 7449. Based on our imaging, RV, and dynamical analysis, the outer companion HD 7449B is most likely a low-mass ($\sim 0.2 M_\odot$) M dwarf orbiting at ~ 18 AU with an eccentricity $\lesssim 0.5$, although larger masses and periods cannot definitively be ruled out by the current data. We have also revised the parameters for the inner planet HD 7449Ab, finding that it is massive and on a very eccentric orbit. We find no evidence for additional planetary companions in the RV data.

Now that HD 7449 is revealed to be a star-planet-M dwarf (SPM) binary, we can place it into relevant context. There are a handful of other SPM systems that consist of a planet orbiting one star with $a < 3$ AU and an M dwarf companion with $a \sim 20$ AU (e.g., HD 196885, Chauvin et al. 2011; γ Cep, Neuhäuser et al. 2007; Gliese 86, Lagrange et al. 2006). HD 7449 is unique among these for three reasons: the secondary component has the lowest mass ($\sim 0.2 M_\odot$ compared to $> 0.4 M_\odot$ for the others), the inner planet is by far the most eccentric (0.8 compared to < 0.5 for the others), and the inner planet is the most massive (nearly double the next most massive). While core accretion is thought to be more difficult in systems like this, it should be possible to grow giant cores within ~ 3 AU (Kley & Nelson 2008). Furthermore HD 7449B’s lower mass would be expected to cause less severe perturbations and thus have fewer detrimental effects on planet formation in the circumstellar disk. Perhaps this explains how the inner planet grew so massive compared to the planets in the other similar systems.

How did the inner planet acquire such a large eccentricity? One possibility is the Kozai mechanism (Kozai 1962; Wu & Murray 2003). If the planet and outer companion were initially on mutually-inclined orbits of at least 39.2° , then the planet’s eccentricity and inclina-

tion would oscillate with oppositely-occurring minima and maxima (Holman et al. 1997). Based on the nominal parameters for the planet and M dwarf companion, the length of a Kozai cycle would be \sim a few hundred years, which is certainly short enough to be plausible given the age of the system (~ 2 Gyr).

Assuming Kozai cycles are responsible, we can use the planet’s current high eccentricity to constrain both the initial and current mutual inclination (Δi_{init} and Δi). It can be shown that if the planet’s orbit is initially circular, the maximum eccentricity is given by $e_{max} = \sqrt{1 - 5/3 \cos^2 \Delta i_{init}}$ (Fabrycky & Tremaine 2007). For $e_{max} = 0.8$, Δi_{init} is constrained to be $\gtrsim 62^\circ$. During Kozai cycles, the quantity $\sqrt{1 - e^2} \cos i$ of the planet is conserved. Using this relation, and the previous constraint on the initial mutual inclination, the current mutual inclination must be $\gtrsim 38^\circ$.

We can carry these constraints one step further. We know that the orbital inclination of the outer companion i_B must be $> 8.4^\circ$ from our MCMC analysis (Section 3.7) and that the current mutual inclination $\Delta i > 38^\circ$ if the planet was initially on a circular orbit and has been undergoing Kozai oscillations. Therefore, under these assumptions, i_b must be $\gtrsim 46.4^\circ$. Plugging this into $m \sin i_b = 7.8 M_J$, the mass of HD 7449Ab would be $\lesssim 10.8 M_J$, ruling out the possibility that it is a low-mass brown dwarf.

Another explanation for the planet’s large eccentricity is planet-planet scattering in the inner parts of the system (e.g., Rasio & Ford 1996). In this case, one or more planets may have been ejected from the system, leaving behind the eccentric HD 7449Ab. This scattering scenario would require both the surviving planet and the scattered planet to be relatively massive ($7\text{--}10 M_J$) and the eccentricity damping of the original circumstellar disk to be small (Moorhead & Adams 2005). Given the “smoking gun” (the nearby M dwarf companion), it seems more likely that Kozai cycles are responsible.

The inner planet’s high eccentricity and small perihelion distance (0.47 AU) raise the possibility of tidal circularization. However, its long period prevents it from circularizing on timescales shorter than $\sim 10^{15}$ years (Adams & Laughlin 2006), meaning that it should continue to undergo Kozai oscillations for the foreseeable future.

This interesting system should continue to be monitored by both RV and imaging. The latter technique, in particular, can provide additional constraints on HD 7449B’s orbit, potentially leading to estimates of its dynamical mass (Crepp et al. 2014). Its eccentricity and inclination could also be further constrained, which could in turn help further constrain the inner planet’s inclination. This would then allow for estimates of the inner planet’s true mass, which is still a sparsely-measured parameter for exoplanets.

High-resolution spectroscopy would help narrow down the effective temperature and spectral type of HD 7449B. While somewhat circular, this could be used to refine the photometry-derived mass ($0.1\text{--}0.2 M_\odot$), which then would affect the possible orbital configurations. For example, excluding RV solutions (from Section 3.7) that have mass $> 0.5 M_\odot$ leads to a median semimajor axis of ~ 15 AU. Excluding masses $> 0.35 M_\odot$ corresponds to

a median semimajor axis of ~ 13 AU. Such small orbits would make HD 7449 a very tightly packed system with vigorous dynamical interactions and would require even more stringent constraints on the outer companion's eccentricity. Specifically, based on additional numerical N-body simulations we performed (using the same approach as described in Section 3.8), the eccentricity would have to be $\lesssim 0.3$ in these cases.

Finally, the companion HD 7449B is interesting because it can become a benchmark object for future studies of stellar structure. The system represents a (still rare) case of an M dwarf with a measured age (via the primary) and a soon-to-be measured mass (via astrometric monitoring). The object's metallicity can be inferred from the primary's or could also be estimated using high-resolution spectroscopy. These quantities together can then help improve stellar structure models for similar cool stars (e.g., Baraffe et al. 2015), for which significant

uncertainties still remain.

We thank the anonymous referee for helpful comments and suggestions. T.J.R. acknowledges support for Program number HST-HF2-51366.001-A, provided by NASA through a Hubble Fellowship grant from the Space Telescope Science Institute, which is operated by the Association of Universities for Research in Astronomy, Incorporated, under NASA contract NAS5-26555. Support for the D.M. is provided by the BASAL CATA Center for Astrophysics and Associated Technologies through grant PFB-06, by the Ministry for the Economy, Development, and Tourism's Programa Iniciativa Científica Milenio through grant IC120009, awarded to the Millennium Institute of Astrophysics (MAS), and by FONDECYT No. 1130196.

REFERENCES

- Adams, F. C., & Laughlin, G. 2006, *ApJ*, 649, 1004
 Anglada-Escudé, G., & Butler, R. P. 2012, *ApJS*, 200, 15
 Anglada-Escudé, G., López-Morales, M., & Chambers, J. E. 2010, *ApJ*, 709, 168
 Anglada-Escudé, G., Arriagada, P., Tuomi, M., et al. 2014, *MNRAS*, 443, L89
 Arriagada, P., Anglada-Escudé, G., Butler, R. P., et al. 2013, *ApJ*, 771, 42
 Baluev, R. V. 2009, *MNRAS*, 395, 1541
 Baraffe, I., Chabrier, G., Allard, F., & Hauschildt, P. H. 1998, *A&A*, 337, 403
 —. 2002, *A&A*, 382, 563
 Baraffe, I., Homeier, D., Allard, F., & Chabrier, G. 2015, *A&A*, 577, A42
 Bernstein, R., Shectman, S. A., Gunnels, S. M., Mochnacki, S., & Athey, A. E. 2003, in *Society of Photo-Optical Instrumentation Engineers (SPIE) Conference Series*, Vol. 4841, Instrument Design and Performance for Optical/Infrared Ground-based Telescopes, ed. M. Iye & A. F. M. Moorwood, 1694–1704
 Bonfanti, A., Ortolani, S., Piotto, G., & Nascimbeni, V. 2015, *A&A*, 575, A18
 Butler, R. P., Marcy, G. W., Williams, E., et al. 1996, *PASP*, 108, 500
 Carpenter, J. M. 2001, *AJ*, 121, 2851
 Chambers, J. E. 1999, *MNRAS*, 304, 793
 Chauvin, G., Beust, H., Lagrange, A.-M., & Eggenberger, A. 2011, *A&A*, 528, A8
 Close, L. M., Gasho, V., Kopon, D., et al. 2010, in *Society of Photo-Optical Instrumentation Engineers (SPIE) Conference Series*, Vol. 7736, Society of Photo-Optical Instrumentation Engineers (SPIE) Conference Series
 Crane, J. D., Shectman, S. A., Butler, R. P., et al. 2010, in *Society of Photo-Optical Instrumentation Engineers (SPIE) Conference Series*, Vol. 7735, Society of Photo-Optical Instrumentation Engineers (SPIE) Conference Series
 Crepp, J. R., Johnson, J. A., Howard, A. W., et al. 2014, *ApJ*, 781, 29
 —. 2013a, *ApJ*, 774, 1
 —. 2012, *ApJ*, 761, 39
 —. 2013b, *ApJ*, 771, 46
 Delgado Mena, E., Bertrán de Lis, S., Adibekyan, V. Z., et al. 2015, *A&A*, 576, A69
 Dumusque, X., Lovis, C., Ségransan, D., et al. 2011, *A&A*, 535, A55
 Dupuy, T. J., & Liu, M. C. 2012, *ApJS*, 201, 19
 Fabrycky, D., & Tremaine, S. 2007, *ApJ*, 669, 1298
 Faherty, J. K., Rice, E. L., Cruz, K. L., Mamajek, E. E., & Núñez, A. 2013, *AJ*, 145, 2
 Faherty, J. K., Burgasser, A. J., Walter, F. M., et al. 2012, *ApJ*, 752, 56
 Ford, E. B. 2005, *AJ*, 129, 1706
 Holman, M., Touma, J., & Tremaine, S. 1997, *Nature*, 386, 254
 Howard, A. W., Johnson, J. A., Marcy, G. W., et al. 2010, *ApJ*, 721, 1467
 Janson, M., Apai, D., Zechmeister, M., et al. 2009, *MNRAS*, 399, 377
 Kley, W., & Nelson, R. P. 2008, *A&A*, 486, 617
 Kopon, D., Close, L. M., Males, J., Gasho, V., & Follette, K. 2010, in *Society of Photo-Optical Instrumentation Engineers (SPIE) Conference Series*, Vol. 7736, Society of Photo-Optical Instrumentation Engineers (SPIE) Conference Series
 Kozai, Y. 1962, *AJ*, 67, 591
 Kraus, A. L., & Hillenbrand, L. A. 2007, *AJ*, 134, 2340
 Lagrange, A.-M., Beust, H., Udry, S., Chauvin, G., & Mayor, M. 2006, *A&A*, 459, 955
 Lucy, L. B. 2014, *A&A*, 563, A126
 Mamajek, E. E., & Hillenbrand, L. A. 2008, *ApJ*, 687, 1264
 Marois, C., Lafrenière, D., Doyon, R., Macintosh, B., & Nadeau, D. 2006, *ApJ*, 641, 556
 Mason, B. D., Hartkopf, W. I., Raghavan, D., et al. 2011, *AJ*, 142, 176
 Minniti, D., Butler, R. P., López-Morales, M., et al. 2009, *ApJ*, 693, 1424
 Montet, B. T., Crepp, J. R., Johnson, J. A., Howard, A. W., & Marcy, G. W. 2014, *ApJ*, 781, 28
 Moorhead, A. V., & Adams, F. C. 2005, *Icarus*, 178, 517
 Morzinski, K. M., Males, J. R., Skemer, A. J., et al. 2015, *ArXiv e-prints*, arXiv:1511.02894
 Neuhäuser, R., Mugrauer, M., Fukagawa, M., Torres, G., & Schmidt, T. 2007, *A&A*, 462, 777
 Pinheiro, F. J. G., Fernandes, J. M., Cunha, M. S., et al. 2014, *MNRAS*, 445, 2223
 Rasio, F. A., & Ford, E. B. 1996, *Science*, 274, 954
 Reid, I. N., & Gizis, J. E. 1997, *AJ*, 113, 2246
 Rodigas, T. J., & Hinz, P. M. 2009, *ApJ*, 702, 716
 Rodigas, T. J., Males, J. R., Hinz, P. M., Mamajek, E. E., & Knox, R. P. 2011, *ApJ*, 732, 10
 Rodigas, T. J., Stark, C. C., Weinberger, A., et al. 2015, *ApJ*, 798, 96
 Roell, T., Neuhäuser, R., Seifahrt, A., & Mugrauer, M. 2012, *A&A*, 542, A92
 Roeser, S., Demleitner, M., & Schilbach, E. 2010, *AJ*, 139, 2440
 Santos, N. C., Sousa, S. G., Mortier, A., et al. 2013, *A&A*, 556, A150
 Scargle, J. D. 1982, *ApJ*, 263, 835
 Schnupp, C., Bergfors, C., Brandner, W., et al. 2010, *A&A*, 516, A21
 Sivanandam, S., Hinz, P. M., Heinze, A. N., Freed, M., & Breuninger, A. H. 2006, in *Society of Photo-Optical Instrumentation Engineers (SPIE) Conference Series*, Vol. 6269, Society of Photo-Optical Instrumentation Engineers (SPIE) Conference Series
 Torres, G. 1999, *PASP*, 111, 169

Tsantaki, M., Sousa, S. G., Adibekyan, V. Z., et al. 2013, *A&A*, 555, A150
Tuomi, M., & Anglada-Escudé, G. 2013, *A&A*, 556, A111
van Leeuwen, F. 2007, *A&A*, 474, 653

Wittenmyer, R. A., Wang, S., Horner, J., et al. 2013, *ArXiv e-prints*, arXiv:1307.0894
Wu, Y., & Murray, N. 2003, *ApJ*, 589, 605